

# Numerical study of thin UHPC targets response against ballistic impact

M. Bisht<sup>1</sup>✉, M.A. Iqbal<sup>1</sup>, K. Kamran<sup>1</sup>, V. Bratov<sup>2</sup>, N.F. Morozov<sup>2,3</sup>

<sup>1</sup>Department of Civil Engineering, Indian Institute of Technology Roorkee, Roorkee-247667, India

<sup>2</sup>Institute for Problems in Mechanical Engineering, Russian Academy of Sciences, Saint Petersburg, Russia

<sup>3</sup>Department of Theory of Elasticity, Saint Petersburg State University, Saint Petersburg, Russia

✉ bishtm809@gmail.com

**Abstract.** The modelling of concrete and its dynamic strength analysis has been an interesting field which seeks many researchers' attention for the last few decades. The material behavior of concrete in extreme dynamic events like blast and impact calls for the understanding of its dynamic characterization as well which demand a suitable material model that can depict the behavior of concrete under high strain rate, high pressure, and large deformations. One of the most used constitutive material models for concrete is HJC (Holmquist Johnson Cook). This model covers most of the essential features of concrete pertaining to response against blast and impact loads. The objective of this paper is to provide an in-depth assessment of the HJC model implemented in ABAQUS Explicit finite element code. The assessment involves various tests such as compression, tensile and tri-axial tests on a single element followed by validation of the numerical model with the help of ballistic experimental tests available in the open literature. Finally based on the assessment, the HJC material model utility for the behavior of thin i.e.,  $H/d \geq 5$ , UHPC (Ultra High-Performance Concrete) targets against impact loading has been discussed.

**Keywords:** HJC (Holmquist Johnson Cook), UHPC (Ultra High-Performance Concrete), ABAQUS Explicit finite element code, ballistic experimental tests

**Acknowledgements.** Authors gratefully acknowledge the financial support provided by the Department of Science and Technology (DST) India and Russian Foundation for Basic Research (RFBR) Russia through research grant nos. INT/RUS/RFBR/DST-1509-CED for successfully carrying out this work.

**Citation:** Bisht M, Iqbal MA, Kamran K, Bratov V, Morozov NF. Numerical study of thin UHPC targets response against ballistic impact. *Materials Physics and Mechanics*. 2022;50(1): 74-88. DOI: 10.18149/MPM.5012022\_6.

## 1. Introduction

The wide utility of concrete material in many critical structures such as nuclear, defense, and protective structures demand the study of its behavior exposed to extreme loadings. To meet this demand, many studies had been carried out on the concrete behavior under extreme dynamic events such as blast and ballistic impact events in literature [1]. All of the studies consist of either experimental assessment [2-8] or investigation through any available FEM tools [9,10] or analytical models [11,12] or combination of any of these two or more methods [13,14]. The development of commercial FEM tools in the past two decades now make it

© M. Bisht, M.A. Iqbal, K. Kamran, V. Bratov, N.F. Morozov, 2022.

Publisher: Peter the Great St. Petersburg Polytechnic University

This is an open access article under the CC BY-NC 4.0 license (<https://creativecommons.org/licenses/by-nc/4.0/>)

possible to develop a more accurate constitutive material model which is able to produce material behavior in a good agreement to a greater extent. Otherwise, the ballistic impact study was restricted to majorly empirical assessment methods only in which targets were divided into two domains i.e., semi-infinite targets and finite thickness targets. Where, semi-infinite targets were used to investigate the deep penetration process into humongous concrete structures by assuming zero lateral boundary effect whereas, finite target thickness was put to use in the study of projectile perforation.

UHPC being a novel material, all its study by the researchers has been majorly done in the last two decades only and are still in progress. Three types of commercially produced concrete having nominal unconfined compressive strength as 35.75 and 110 MPa were cast in order to perform the ballistic impact tests on 50 mm thick targets impacted against by 20 mm diameter ogival nosed steel projectiles. The ballistic impact tests were then examined in terms of the ballistic limit curve and its velocity for each concrete type. Furthermore, various material tests were also conducted to examine the mechanical properties of the concrete. Finally, the Modified HJC material model was calibrated and validated with the experimental ballistic perforation results in good agreement through LS Dyna FEM tool [15].

Ballistic perforation tests had been carried out on thin 129 MPa UHP-SFRC targets. The range of UHP-SFRC (Ultra High-Performance Steel Fibre Reinforced Concrete) targets thickness varied from 40 mm to 100 mm and the diameter of the projectile was 25.3 mm with a 3 CRH (Caliber Radius Head) ogival nose measured 331 grams in weight. The objective of the study was to capture the residual velocities of normally perforated projectiles with the help of high-speed cameras in order to develop a semi-analytical projectile perforation model for thin concrete slabs i.e.,  $H/d$  is less than or equal to 5. Subsequently, the developed semi-analytical model was validated by the existing available perforation test data on a thin concrete slab. Furthermore, the developed model show results in good agreement when put forward to investigate the ballistic resistance of spaced layered concrete targets [16].

The ballistic impact of UHPCC (Ultra High-Performance Cement-based Composites) developed with steel fibres and basalt coarse aggregates was experimentally evaluated by carrying out very high-velocity projectile penetration tests ranging from 510 m/s to 1320 m/s. It was observed that as the impact velocity go beyond 1000 m/s, the projectile no more behaved like a rigid mass projectile. On the basis of parameters influential analyses, it was observed that the most effective and cost-effective selection for the anti-strike protective structure was UHPCC which was having 90 MPa as compressive strength with 1.5 % of steel fibres in the mix. It was further validated through experimental results that UHPCC performed outstandingly against ballistic impact in terms of reducing the depth of penetration, deviating the terminal ballistic trajectory of the abrasive projectile, and reducing the crater damage dimensions [17].

The study of damage caused by explosion-generated fragments impact had been done through the behavior of several UHPFRC (Ultra High-Performance Fibre Reinforced Concrete) targets against small firearm projectile impact. The range of real ammunition impact velocity was kept between 691 m/s to 720 m/s. Moreover, fibre content in the UHPFRC mix was increased up to 3 % by volume to examine the effect of fibres on the target damage in terms of penetration depth, debris fragment mass, crater diameter, and residual penetration potential of the bullet. On the basis of experimental observations, it was concluded that the optimum fibre amount in the UHPFRC mix came out to be 2 %. Less than 2 % fibres lead to an increased volume of secondary fragments generated from the rear side of the targets and also the residual penetration potential of the small fire ammunition leaving from the rear side of the target was found to be higher. Whereas, more than 2 % fibres showed no significant improvements in all the damage parameters [18].

The experimental impact resistance study of concrete having compressive strength ranging from 45 MPa to 235 MPa was carried out. The concrete targets were impacted by a 12.6 mm ogive nosed projectile with 15 grams in weight at impact velocities ranging from 620 m/s to 700 m/s. It was witnessed that as the compressive strength of the concrete target increased, the penetration depth and crater diameter magnitude decreased with a non-linear trend. Moreover, the presence of steel fibres did not show any substantial influence on penetration depth unlike the presence of coarse granite aggregates. However, both steel fibres, as well as coarse granite aggregates, proved to be advantageous in order to minimize the crater diameter and crack propagation thereby increasing the impact resistance. Finally, it was concluded that the most effective anti-strike protective high-strength fibre reinforced concrete target was the one which was having compressive strength of 100 MPa [19].

The study of novel UHPC behavior under extreme dynamic events like blast and impact loadings is a new field for many researchers across the globe because of its high capacity to absorb energy, greater resistance to impact loadings, being a novel material [20-22] and high utility in major infrastructure susceptible to dynamic loadings are the few reasons out of many. This present paper aims to provide in-depth evaluation of the HJC material model implemented in ABAQUS Explicit finite element code in order to find its utility for the UHPC behavior under impact dynamic loading.

## 2. Constitutive Material Model: HJC

The HJC [23] material model was developed by Holmquist, Johnson, and Cook in 1993 in order to describe the dynamic behavior of concrete subjected to high pressures, high strain rates, and large deformations. It is an elastic-viscoplastic model and consists of three components as Strength, Damage, and Equation of State model. All three model components are briefly described below one by one:

**Strength Model** is an illustration of the intact and fractured material's normalized deviatoric strength in the form of normalized pressure-dependent yield surface as shown in Fig. 1. The normalized deviatoric strength can be given as the function of the pressure and strain rate as

$$\sigma^* = [A(1-D) + B(P^*)^N] [1 + C \ln(\dot{\epsilon}^*)] \leq S_{max}, \quad (1)$$

where  $\sigma^*$  is the normalized deviatoric strength.

Further, ABAQUS Explicit finite element code assumes plastic flow to be isochoric i.e., volume-preserving using a Mises flow surface.

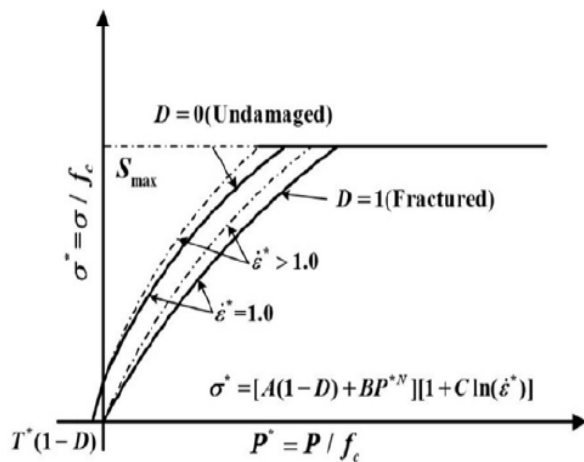


Fig. 1. Strength of HJC model [24]

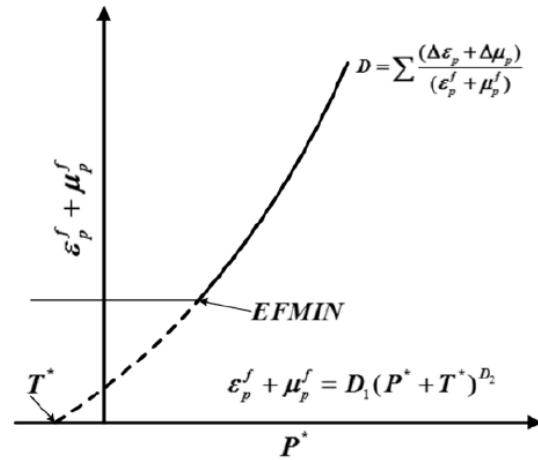


Fig. 2. Damage of HJC model [24]

**Damage Model** explains how the damage variable accumulates with the equivalent plastic strain and volumetric plastic strain as shown in Fig. 2. Moreover, the concrete material can not undergo any plastic strain at  $P^*$  equals to  $T^*$ , and plastic strain to fracture increases as  $P^*$  increases. Whereas, in order to suppress fracture from low magnitude tensile waves, EFMIN is introduced which allows for a finite amount of plastic strain to fracture the material. Although, under most conditions, the majority of the damage would occur only from equivalent plastic strain damage due to plastic volumetric strain is also included in this model to take into account the loss of cohesive strength during air void collapse.

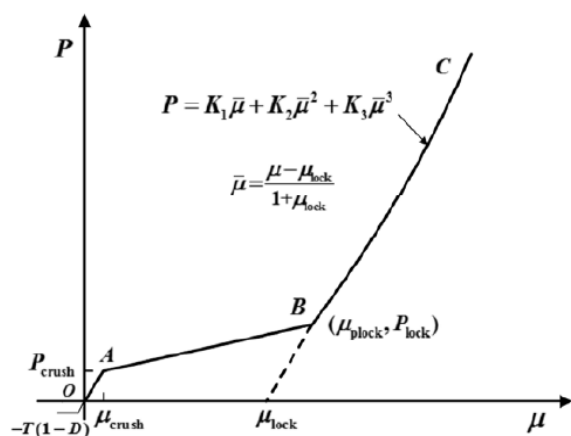


Fig. 3. EOS of HJC model [24]

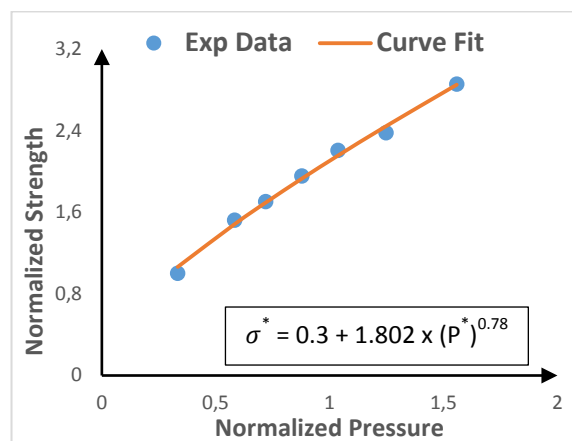


Fig. 4. HJC-Strength Model Curve fit

Table 1. HJC material model parameters used in the present study

Material Parameters	Numerical Value
Density ( $\text{kg/m}^3$ )	2600
Shear Modulus (GPa)	22
<b>Strength Model</b>	<b>HJC</b>
Normalized Cohesive strength, A	0.3
Normalized pressure hardening coefficient, B	1.802
Pressure hardening exponent, N	0.78
Strain rate coefficient, C	0.005
Quasi-static uniaxial compression strength, $f_{ck}$ (GPa)	0.129
Normalized maximum strength, $S_{max}$	3.5
<b>Damage Model</b>	<b>HJC</b>
Parameter for plastic strain to fracture, $D_1$	0.04
Parameter for plastic strain to fracture (exponent), $D_2$	1
<b>Equation of State</b>	<b>Polynomial</b>
Pressure at crushing, $P_{crush}$ (GPa)	0.043
Volumetric strain at crushing, $\mu_{crush}$	0.001
Pressure at fully compaction, $P_{lock}$ (GPa)	3.47
Volumetric strain at fully compaction, $\mu_{lock}$	0.11
First pressure coefficient, $K_1$ (GPa)	116
Second pressure coefficient, $K_2$ (GPa)	-243
Third pressure coefficient, $K_3$ (GPa)	506
Maximum tensile hydrostatic pressure, T (GPa)	0.006

**Equation of State Model** explains the pressure-volume response of the material under compression as shown in Fig. 3. The response is divided into three regions. The first region

depicts the linear elastic behavior. The second region depicts the linear inelastic behavior or also refer as the transition region. In this region, the air voids are progressively expelled out of the concrete resulting in volumetric plastic strain. And the third region represents the fully compacted material behavior through the cubic polynomial equation. In this region, no air voids are left in the concrete matrix.

**HJC material model parameters** Assuming 'A' as 0.3, HJC strength model parameters  $B$  and  $N$  are confirmed as 1.802 and 0.78 respectively through curve fitting of experimental Tri-axial tests data [25] as shown in Fig. 4 by neglecting strain rate effect i.e., 'C' equals to 0. All the other model parameters are taken directly from available literature [24]. Readers are advised to refer [23,24] in order to get more insight into the procedure for determining the material constants. Table 1 shows all the HJC material model parameters used for UHPC material in the present numerical study.

### 3. Numerical Study

In this section of the paper, numerical study on HJC material model implemented in ABAQUS Explicit FEM code has been carried out. This is done by performing various tests on a single element required to examine the HJC material model. Furthermore, a numerical model is also developed to validate the experimental ballistic test results through HJC material model. Finally, the results obtained from the numerical study are discussed and concluded.

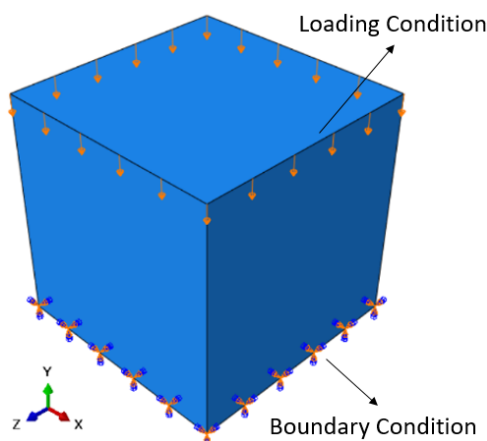


**Fig. 5.** Boundary conditions for compression test on a single element

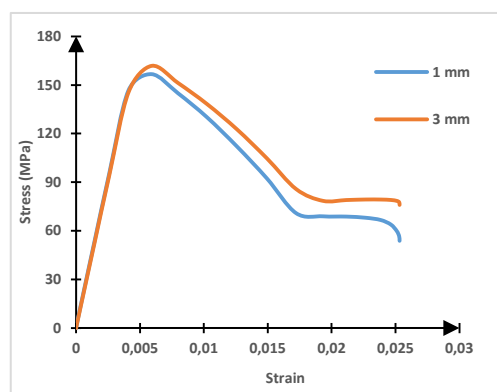


**Fig. 6.** Compression stress-strain curve

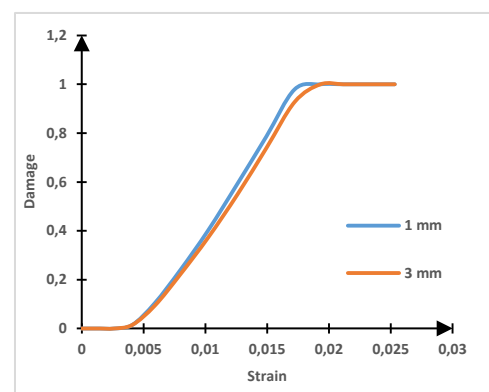


**Fig. 7.** Evolution of damage

**Compression Tests** on 1 mm and 3 mm C3D8R (Continuum 3 Dimensional 8 Node Reduced Integrated) single element are carried out separately. The boundary conditions of the single element are shown in Fig. 5 in which translational and rotational motion of the bottom

plane surface is restricted in all directions and the compression loading is provided through the downward displacement of the top surface. The stress-strain curve of a single element under compression is shown in Fig. 6 and the development of damage in the element with respect to strain is shown in Fig. 7. It has been noticed that the developed damage reaches one as the element approaches its critical state or residual stress state. Furthermore, no significant difference is observed in the stress-strain curve of 1 mm and 3 mm C3D8R single element under compression.

**Tri-axial Tests** on 1 mm C3D8R single element are carried out at various confinement pressure. The boundary conditions of a single element under the Tri-axial test are shown in Fig. 8 in which translational and rotational motion of the bottom plane surface is restricted in all directions, an instantaneous pressure load is provided on all the surfaces followed by the downward displacement loading on the top surface. The stress-strain curves of a single element under the Tri-axial test at four various confinement pressure obtained from numerical study are shown in Fig. 10. Tri-axial numerical test results at four various confinement pressure are found to be in good agreement with Ren et al. [25] experimental test results as shown in Fig. 9. Although a significant difference in the numerical strength result when compared to the experimental strength result is detected at the unconfined i.e., 0 MPa Tri-axial test or simple compression test as shown in Fig. 11.

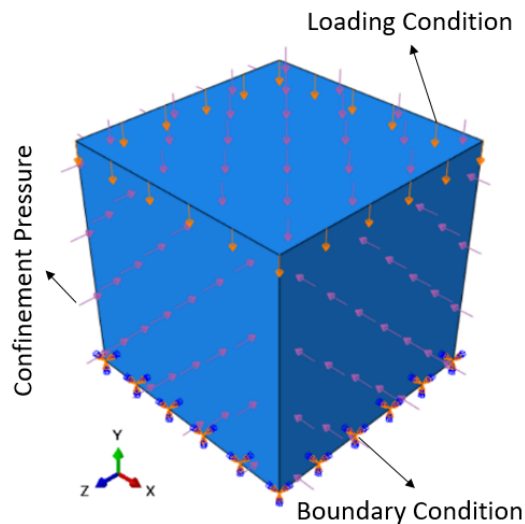


**Fig. 8.** Boundary conditions for tri-axial test on a single element

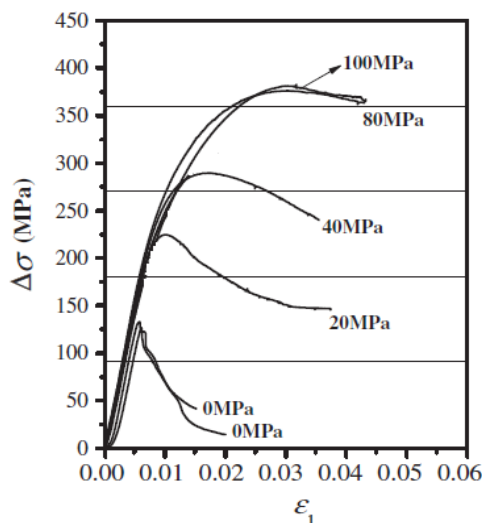


**Fig. 9.** Exp. Tri-axial stress-strain curve [25]

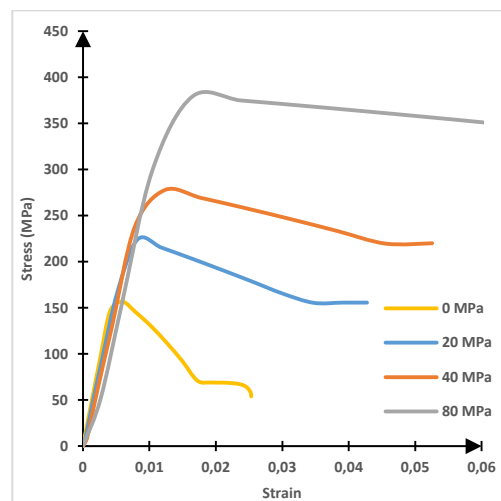


**Fig. 10.** Num. Tri-axial stress-strain curve

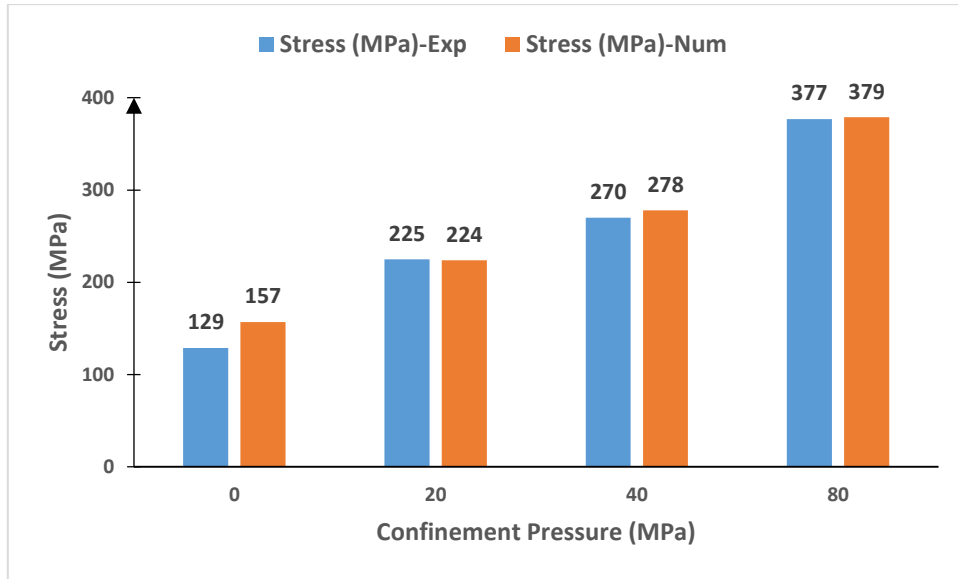


**Fig. 11.** Comparison of Exp. & Num. Tri-axial test results

**Tensile Test** on 1 mm C3D8R single element is carried out. The boundary conditions of the single element are shown in Fig. 12 in which translational and rotational motion of the bottom plane surface is restricted in all directions and the tensile loading is provided through the upward displacement of the top surface. The stress-strain curve of a single element under tensile loading is shown in Fig. 13 and the evolution of damage in the element with respect to strain is shown in Fig. 14. Similar to the unconfined compression test results, here also numerical study result overestimates the experimental study result since the tensile strength input in HJC material model is 6 MPa.

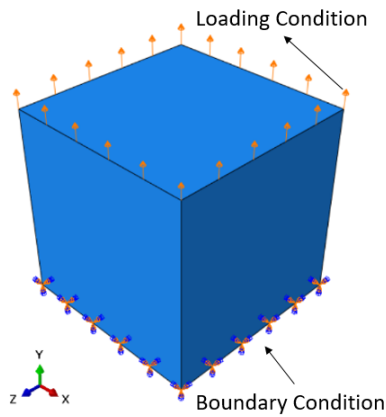


**Fig. 12.** Boundary conditions for tensile test on a single element

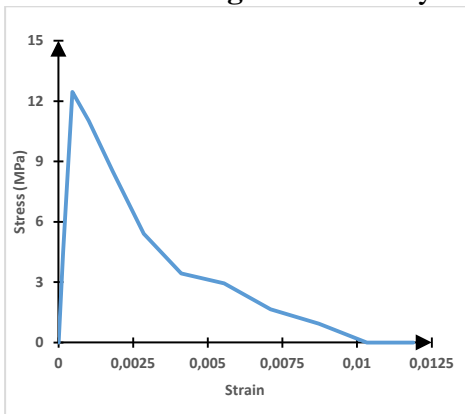


**Fig. 13.** Tensile stress-strain curve

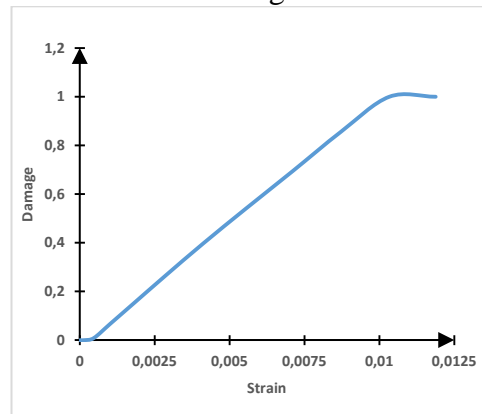


**Fig. 14.** Evolution of damage

**Validation** The numerical model validation is done with the help of Peng et al. ballistic study [16]. He had carried out a projectile perforation test on the thin UHP-SFRC slabs, in which the diameter of the projectile was 25.3 mm and the thicknesses of slabs ranged from 40 mm to 70 mm. All the slabs were perforated normally and the projectile residual velocities were captured by a high-speed camera.

In the developed numerical model, HJC constitutive material model is used for UHP-SFRC targets whereas, the analytical rigid material model is assigned to the steel projectile as no deformation was observed in the projectiles after perforation in the ballistic tests. UHP-SFRC targets having a clear arial dimension of  $400 \times 400$  mm with thickness ranging from 40 mm to 70 mm were impacted by 331 grams, 3.0-caliber radius head ogival nose steel projectile with 25.3 mm shank diameter and total length of 152 mm. Surface-to-surface interaction with kinematic contact algorithm has been provided between the steel projectile and UHP-SFRC target. The peripheral surface edges of UHP-SFRC targets are constrained with respect to all translational and rotational movement as shown in Fig. 15. The UHP-SFRC targets are modelled with linear C3D8R elements of size  $1.5 \times 1.5 \times 1.5$  mm, as shown in Fig. 16. Whereas, no meshing has been provided to steel projectile due to its analytical rigid material model.

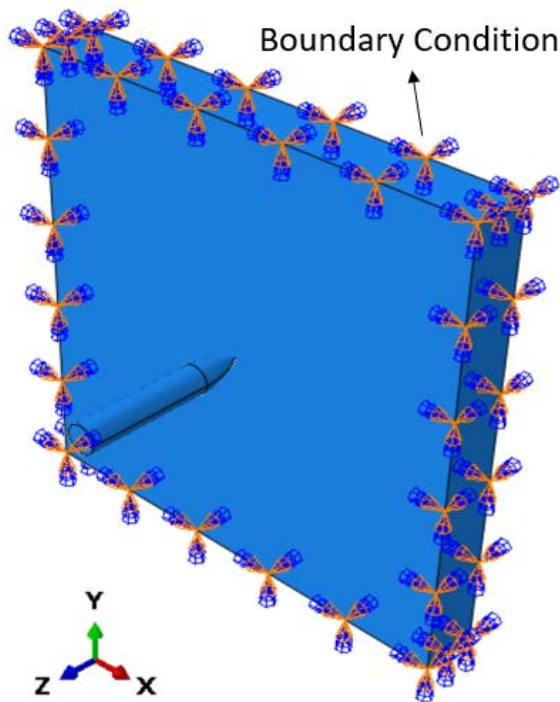


**Fig. 15.** Numerical model

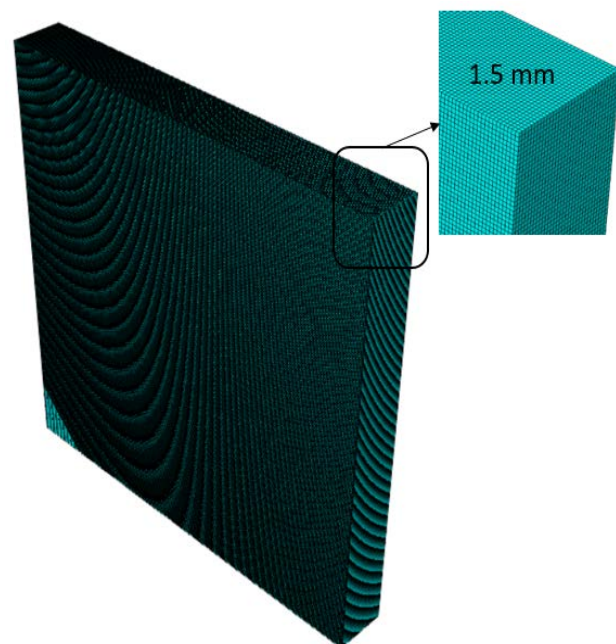


**Fig. 16.** Mesh on Numerical model

Figures 17 and 18 show the comparison between experimental and numerical model damage on the front and the rear surface of 40 and 70 mm UHP-SFRC targets against steel projectile with 352 and 348 m/s impact velocities respectively. The diameter of the front and the rear damages obtained from experimental ballistic test are found to be 62.3 and 106 mm on 40 mm thick target and 107 and 129 mm on 70 mm thick target respectively. Whereas, the diameter of the front and the rear damages obtained from numerical ballistic test are found to be 85 and 119 mm on 40 mm target and 98 and 150 mm on 70 mm thick target respectively.

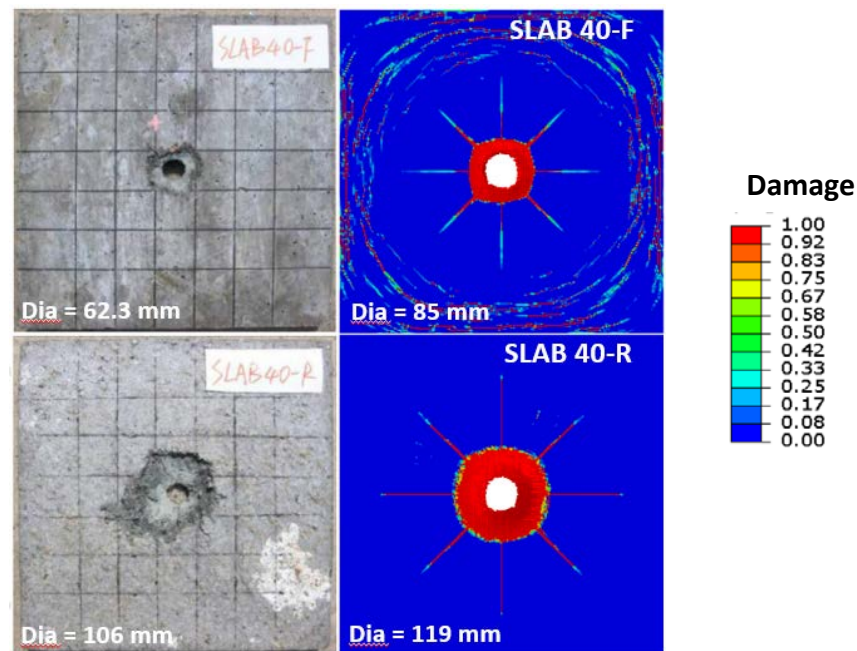


**Fig. 17.** Experimental and numerical model damage on the front (F) and the rear (R) of 40 mm UHP-SFRC targets @ 352 m/s impact velocity

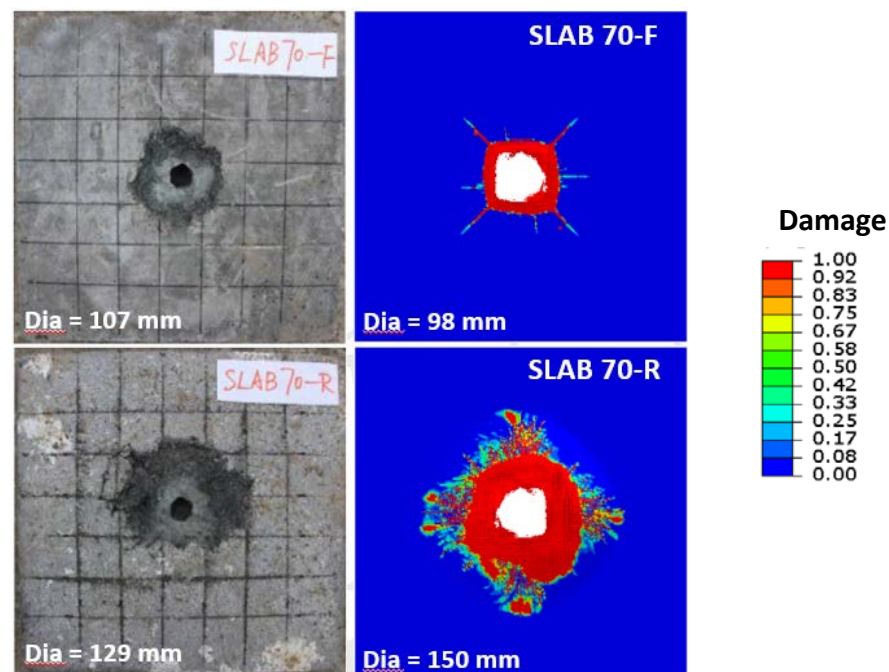


**Fig. 18.** Experimental and numerical model damage on the front (F) and the rear (R) of 70 mm UHP-SFRC targets @ 348 m/s impact velocity

Table 2 shows the ballistic perforation results obtained from the numerical study which are in very good agreement with respect to the experimental study as the maximum error was found to be 2.92 % for 50 mm thick UHP-SFRC at 250 m/s impact velocity. Moreover, Figure 19 shows the comparison between experimental and numerical ballistic perforation results of 50 mm thick targets against steel projectile impact in terms of residual velocities corresponding to various impact velocities i.e., 250, 347, and 478 m/s through a histogram plot. Similarly, Figure 20 shows the comparison between experimental and numerical ballistic perforation results of 40, 50, 60, and 70 mm thick targets against steel projectile impact in

terms of residual velocities corresponding to 352, 347, 341, and 348 m/s impact velocities respectively through histogram plot.

Table 2. Ballistic Perforation Results of 40, 50, 60, and 70 mm thick UHP-SFRC targets

Thickness	Impact Velocity (m/s)	Residual Velocity (m/s)		
		Exp	Num	Error (%)
50 mm	250	171	176	2.92
	347	283	280	-1.06
	478	425	416	-2.12
40 mm	352	305	303	-0.66
60 mm	341	251	248	-1.20
70 mm	348	232	232	0.00

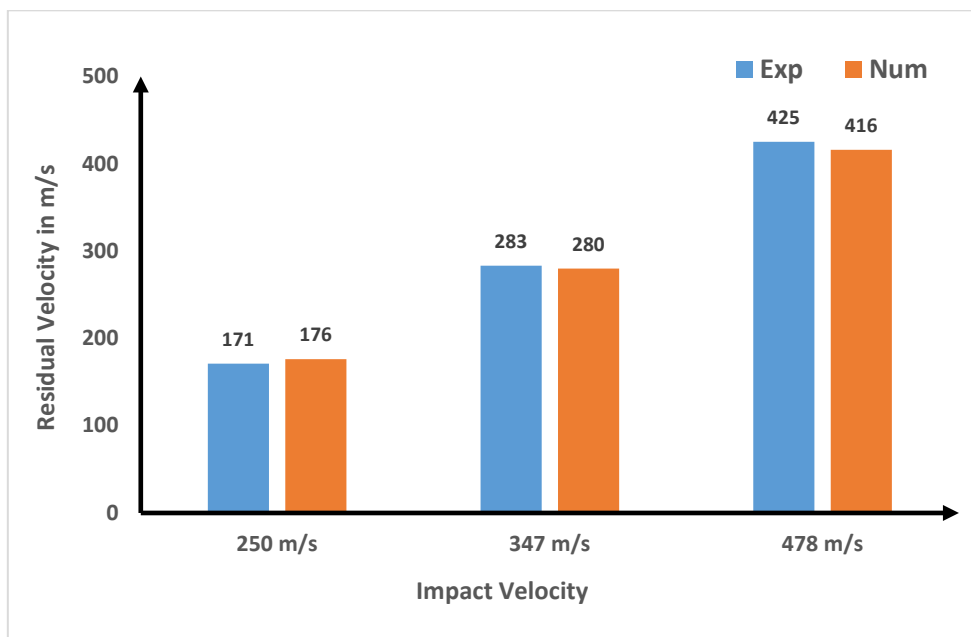


Fig. 19. Ballistic perforation results of 50 mm targets

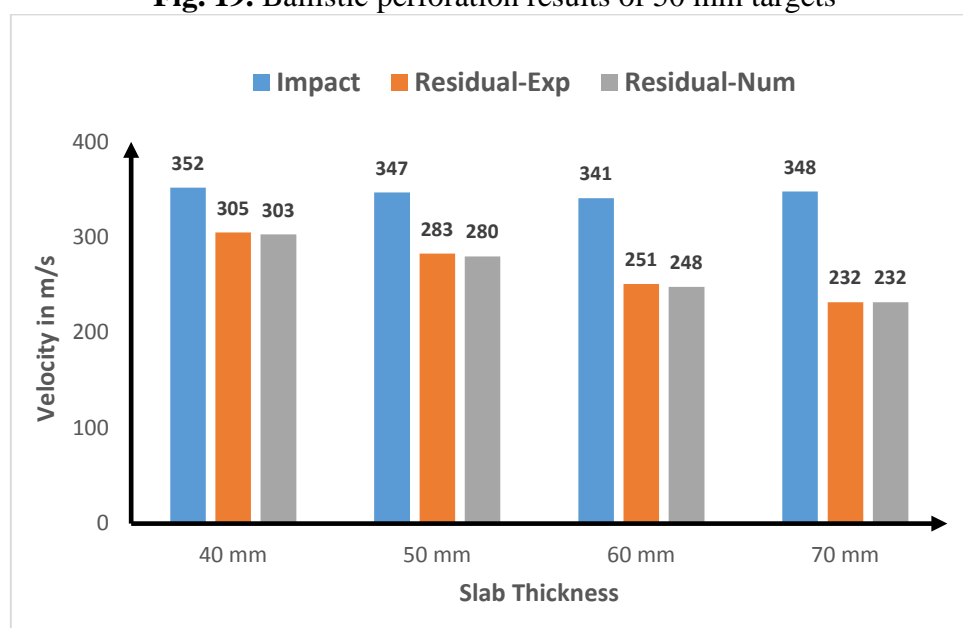
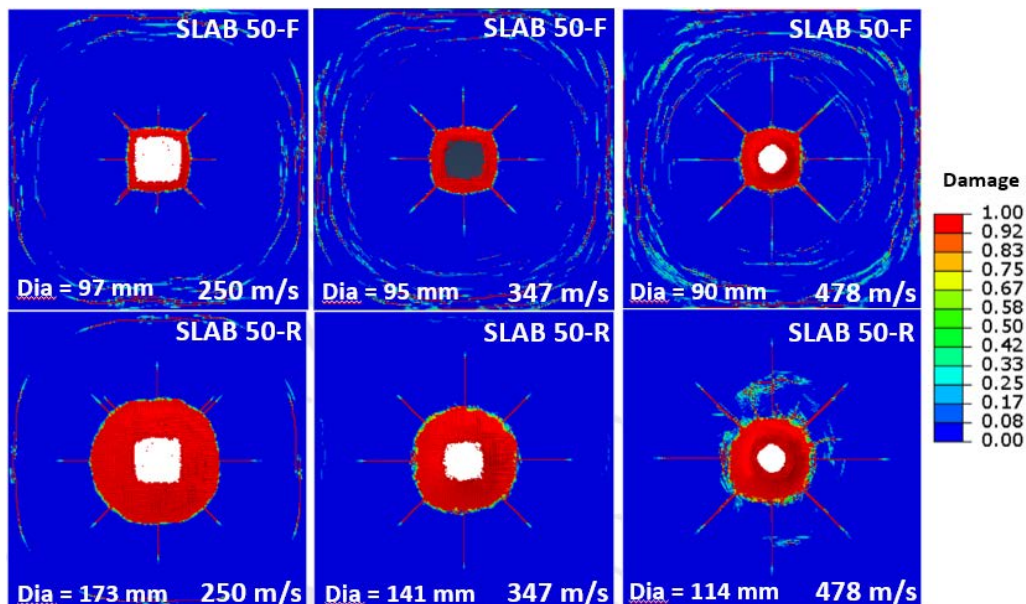
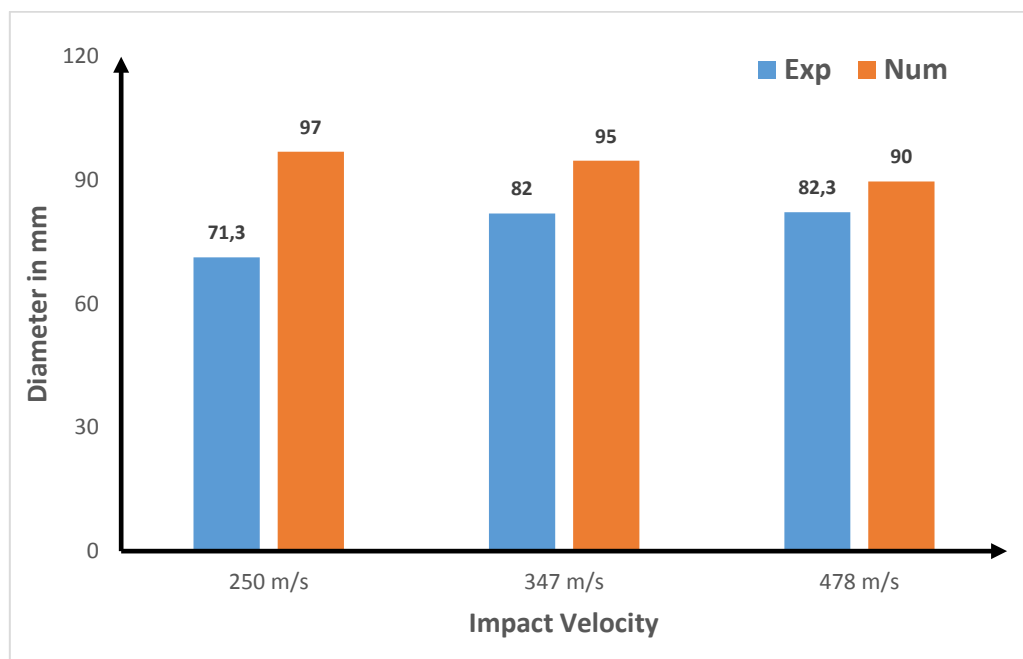


Fig. 20. Ballistic perforation results of 40, 50, 60, and 70 mm targets

Figure 21 shows damage on the front and the rear surface of 50 mm UHP-SFRC targets against steel projectile obtained from the numerical study at 250, 347, and 478 m/s impact velocities. The diameter of the front and the rear surface damages are found to be 97 mm and 173 mm at 250 m/s impact velocity, 95 mm and 141 mm at 347 m/s impact velocity, and 90 mm and 114 mm at 478 m/s impact velocity. It is observed that the nature of the damage gets transformed from global to local as the impact velocity increases from 250 to 478 m/s. This is because of the fact that as the impact velocity increases, the duration of loading decreases, and thus the whole target does not get sufficient time to respond against it. As a result, only the portion which is near in the vicinity of the fast-moving steel projectile responds and gets damaged.



**Fig. 21.** Numerical model damage on the front (F) and the rear (R) of 50 mm UHP-SFRC targets at 250, 347, and 478 m/s impact velocity



**Fig. 22.** Front damage crater diameter of 50 mm targets

Figures 22 and 23 show histogram plot comparison between experimental and numerical study's damage on the front and the rear surface of 50 mm thick UHP-SFRC targets at various impact velocities respectively. It has been noticed that as the impact velocity increases the damage results obtained from numerical study converge to damage results obtained from the experimental study. The local damage in the experimental study can be attributed to the steel fibres present in the UHP-SFRC targets, as the steel fibres do not allow cracks to propagate further thus restricting the damage to the near vicinity of the moving steel projectile.

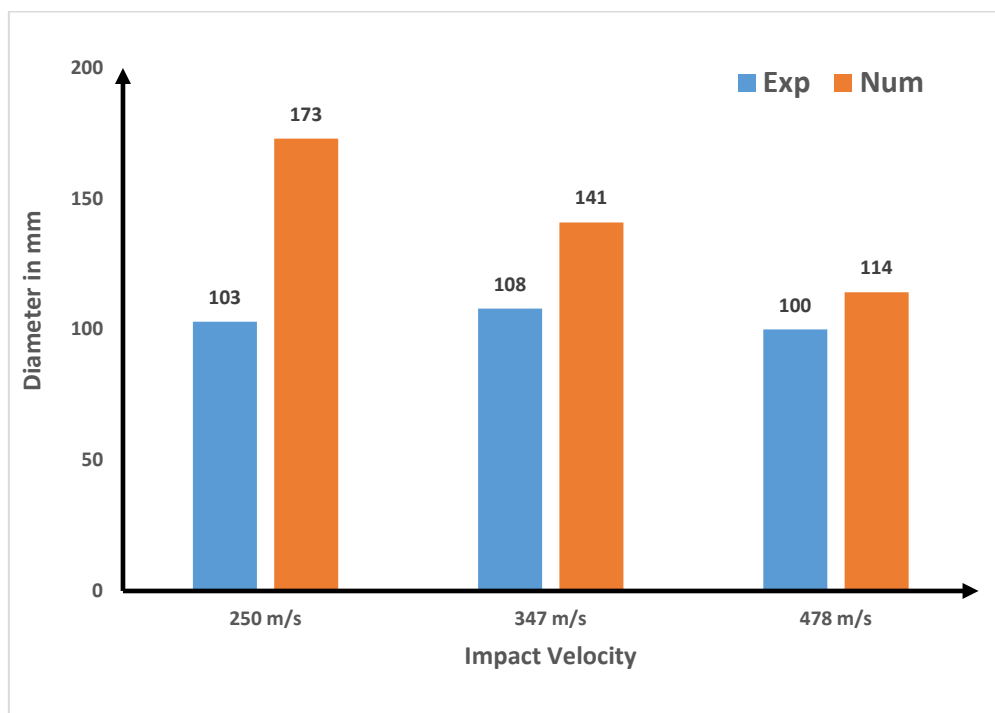


**Fig. 23.** Rear damage crater diameter of 50 mm targets

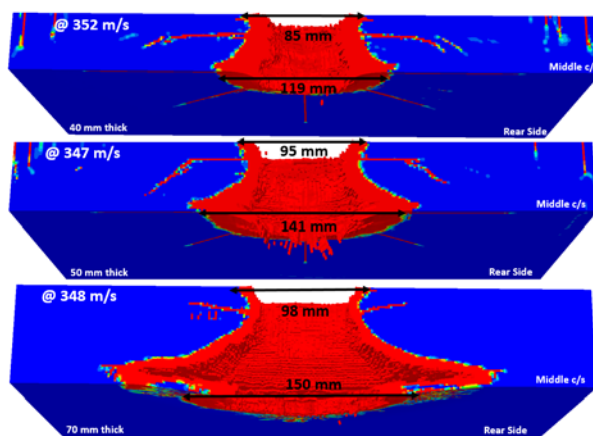


**Fig. 24.** Damage contour of 40, 50, and 70 mm targets at mid c/s against nearly 350 m/s impact velocity

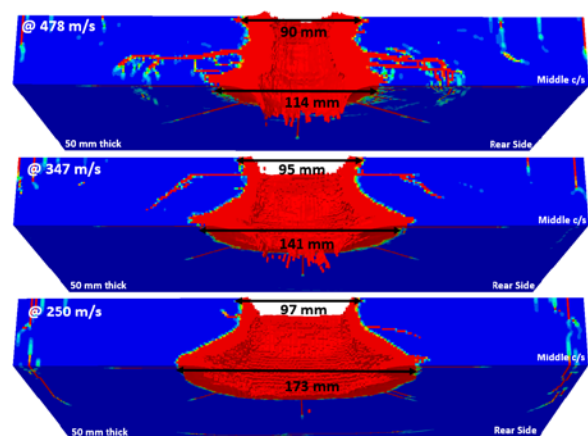


**Fig. 25.** Damage contour of 50 mm targets at mid c/s against 478, 347, and 250 m/s impact velocity

Figure 24 shows the damage contour variations at the mid-cross-section of the target having 40, 50, and 70 mm thickness at nearly 350 m/s impact velocity respectively. Whereas, Figure 25 shows the damage contour variations at the mid-cross-section of 50 mm targets at

various impact velocities i.e., 478, 347, and 250 m/s respectively. The change in the nature of the damage from local to global appears to be the same as the thickness of the target increases (keeping impact velocity constant) or the impact velocity decreases (keeping the thickness of the target constant).

#### 4. Conclusions

In the present paper, a detailed investigation of HJC material model implemented in ABAQUS software has been carried out. Based on the various tests performed on a single element followed by the ballistic tests, the following conclusions are made:

- The unconfined compression and tensile test results obtained from the numerical study overestimate the test results when compared with the experimental study. It indicates that strength definition in the lower confinement zone is not properly defined in HJC-Strength model.
- However, tri-axial test results at various confinement pressure obtained from the numerical study are found to be in good agreement with the experimental study results.
- Further, ballistic perforation results of 40, 50, 60, and 70 mm thick UHP-SFRC targets obtained from the numerical study in terms of residual velocities and their corresponding impact velocities are found to be in good correspondence with the experimental results with a maximum error of 2.92%.
- Although, the nature of the damage on the front and the rear surface has been found to transform from local to global damage as the impact velocity decreases or the thickness of the target increases. It was so because of two reasons. Firstly, ballistic perforation time duration i.e., as the time duration increases, more area of the target able to involve in the damage mechanism. Secondly, bi-linear strain softening of HJC-Tensile strength model does not incorporate the behavior of strain hardening of UHP-SFRC concrete in tension. The strain hardening behavior of UHP-SFRC concrete in tension is due to the presence of steel fibres which create hindrance in the cracks propagation.

#### References

1. Das N, Nanthagopalan P. State-of-the-art review on ultra high performance concrete-Ballistic and blast perspective. *Cement and Concrete Composites*. 2022;127: 104383.
2. Máca P, Sovják R, Konvalinka P. Mix design of UHPFRC and its response to projectile impact. *International Journal of Impact Engineering*. 2014;63: 158-163.
3. Dancygier AN, Yankelevsky DZ, Jaegermann C. Response of high performance concrete plates to impact of non-deforming projectiles. *International Journal of Impact Engineering*. 2007;34(11): 1768-1779.
4. Wang S, Le HT, Poh LH, Feng H, Zhang MH. Resistance of high-performance fiber-reinforced cement composites against high-velocity projectile impact. *International Journal of Impact Engineering*. 2016;95: 89-104.
5. Hanchak SJ, Forrestal MJ, Young ER, Ehrgott JQ. Perforation of concrete slabs with 48 MPa (7 ksi) and 140 MPa (20 ksi) unconfined compressive strengths. *International Journal of Impact Engineering*. 1992;12(1): 1-7.
6. O'Neil EF, Neeley BD, Cargile JD. Tensile properties of very-high-strength concrete for penetration-resistant structures. *Shock and Vibration*. 1999;6(5-6): 237-245.
7. Forrestal MJ, Altman BS, Cargile JD, Hanchak SJ. An empirical equation for penetration depth of ogive-nose projectiles into concrete targets. *International Journal of Impact Engineering*. 1994;15(4): 395-405.
8. Almusallam TH, Siddiqui NA, Iqbal RA, Abbas H. Response of hybrid-fiber reinforced concrete slabs to hard projectile impact. *International Journal of Impact Engineering*. 2013;58: 17-30.

9. Murthy A, Palani GS, Iyer NR. Impact Analysis of Concrete Structural Components. *Defence Science Journal*. 2010;60(3): 307-319.
10. Polanco-Loria M, Hopperstad OS, Børvik T, Berstad T. Numerical predictions of ballistic limits for concrete slabs using a modified version of the HJC concrete model. *International Journal of Impact Engineering*. 2008;35(5): 290-303.
11. Forrestal MJ, Altman BS, Cargile JD, Hanchak SJ. An empirical equation for penetration depth of ogive-nose projectiles into concrete targets. *International Journal of Impact Engineering*. 1994;15(4): 395-405.
12. Li QM, Chen XW. Dimensionless formulae for penetration depth of concrete target impacted by a non-deformable projectile. *International Journal of Impact Engineering*. 2003;28(1): 93-116.
13. Shafieifar M, Farzad M, Azizinamini A. Experimental and numerical study on mechanical properties of Ultra High Performance Concrete (UHPC). *Construction and Building Materials*. 2017;156: 402-411.
14. Tai YS. Flat ended projectile penetrating ultra-high strength concrete plate target. *Theoretical and Applied Fracture Mechanics*. 2009;51(2): 117-128.
15. Kristoffersen M, Toreskås OL, Dey S, Børvik T. Ballistic perforation resistance of thin concrete slabs impacted by ogive-nose steel projectiles. *International Journal of Impact Engineering*. 2021;156: 103957.
16. Peng Y, Wu H, Fang Q, Liu JZ, Gong ZM. Residual velocities of projectiles after normally perforating the thin ultra-high performance steel fiber reinforced concrete slabs. *International Journal of Impact Engineering*. 2016;97: 1-9.
17. Wu H, Fang Q, Chen XW, Gong ZM, Liu JZ. Projectile penetration of ultra-high performance cement based composites at 510–1320 m/s. *Construction and Building Materials*. 2015;74: 188-200.
18. Sovjak R, Vavřinik T, Zatloukal J, Maca P, Mičunek T, Frydrýn M. Resistance of slim UHPFRC targets to projectile impact using in-service bullets. *International Journal of Impact Engineering*. 2015;76: 166-177.
19. Zhang MH, Shim VP, Lu G, Chew CW. Resistance of high-strength concrete to projectile impact. *International Journal of Impact Engineering*. 2005;31(7): 825-841.
20. Graybeal B. *Ultra-high performance concrete*. 2011. Available from: <https://www.fhwa.dot.gov/publications/research/infrastructure/structures/11038/index.cfm>
21. Abdulkareem OM, Fraj AB, Bouasker M, Khelidj A. Mixture design and early age investigations of more sustainable UHPC. *Construction and Building Materials*. 2018;163: 235-246.
22. Abbas SM, Nehdi ML, Saleem MA. Ultra-high performance concrete: Mechanical performance, durability, sustainability and implementation challenges. *International Journal of Concrete Structures and Materials*. 2016;10(3): 271-295.
23. Holmquist TJ, Johnson GR, Cook WH. A computational constitutive model for concrete subjected to large strains, high strain rates, and high pressures. In: *Proceedings of the 14th International Symposium on Ballistics*. 1993.
24. Ren GM, Wu H, Fang Q, Kong XZ. Parameters of Holmquist–Johnson–Cook model for high-strength concrete-like materials under projectile impact. *International Journal of Protective Structures*. 2017;8(3): 352-367.
25. Ren GM, Wu H, Fang Q, Liu JZ, Gong ZM. Triaxial compressive behavior of UHPCC and applications in the projectile impact analyses. *Construction and Building Materials*. 2016;113: 1-4.

**THE AUTHORS****Bisht M.**

e-mail: bishtm809@gmail.com

ORCID: 0000-0001-7322-947X

**Iqbal M.A.**

e-mail: ashraf.iqbal@ce.iitr.ac.in

ORCID: 0000-0002-3428-1395

**Kamran K.**

e-mail: kmrn890@gmail.com

ORCID: 0000-0001-6456-3089

**Bratov V.**

e-mail: vladimir@bratov.com

ORCID: 0000-0003-0564-0800

**Morozov N.F.**

e-mail: morozov@NM1016.spb.edu

ORCID: -